Discover Materials

Research

Ultra-efficient MCF-7 cell ablation and chemotherapy-integrated electrothermal therapy with DOX–WS_2–PEG–M13 nanostructures

Fitya S. Mozar[1] · Maria P. Meivita[1] · Shao-Xiang Go[1] · Lunna Li[2] · Natasa Bajalovic[1] · Desmond K. Loke[1]

Received: 6 October 2023 / Accepted: 20 February 2024
Published online: 27 February 2024

Abstract
Clinical trials have generated encouraging outcomes for the utility of thermal agents (TAs) in cancer thermal therapy (TT). Although the fast breakdown of TAs alleviates safety concerns, it restricts the thermal stability necessary for effective treatment. TAs with excellent thermal stability, on the other hand, deteriorate slowly. Rare are the approaches that address the trade-off between high thermal stability and quick deterioration of TAs. Here we control the thermal signature of WS_2-type 2D materials by utilizing previously undescribed DOX–WS_2–PEG–M13 nanostructures (we term them D nanostructures) through Joule heating phenomena, and develop an integrated system for TT for enhancing thermal performance, and simultaneously, maintaining rapid degradation, and chemotherapy for efficacious treatment. A relative cell viability of ~ 50% was achieved by the D-based TT (DTT) configuration, as well as a 1 nM drug concentration. The D-driven chemotherapy (DCT) model also attains a relative cell viability of 80% for 1 nM drug concentration, while a 1-week degradation time was revealed by the D nanostructure. Theoretical studies elucidate the drug molecule–nanostructure and drug-on-nanostructure–solution interaction-facilitated enhancement in drug loading and drug release performance in DCT varieties. As a result, this work not only proposes a "ideal TA" that circumvents TA restrictions, but also enables proof-of-concept application of WS_2-based materials in chemotherapy-unified combination cancer therapy.

Supplementary Information The online version contains supplementary material available at https://doi.org/10.1007/s43939-024-00076-8.

✉ Natasa Bajalovic, natasa_bajalovic@sutd.edu.sg; ✉ Desmond K. Loke, desmond_loke@sutd.edu.sg; Fitya S. Mozar, syarifa_mozar@sutd.edu.sg; Maria P. Meivita, maria_meivita@mymail.sutd.edu.sg; Shao-Xiang Go, shaoxiang_go@mymail.sutd.edu.sg; Lunna Li, syndia02@gmail.com | [1]Department of Science, Mathematics and Technology, Singapore University of Technology and Design, Singapore 487372, Singapore. [2]Department of Chemical Engineering, Thomas Young Centre, University College London, London WC1E 7JE, UK.

Graphical Abstract

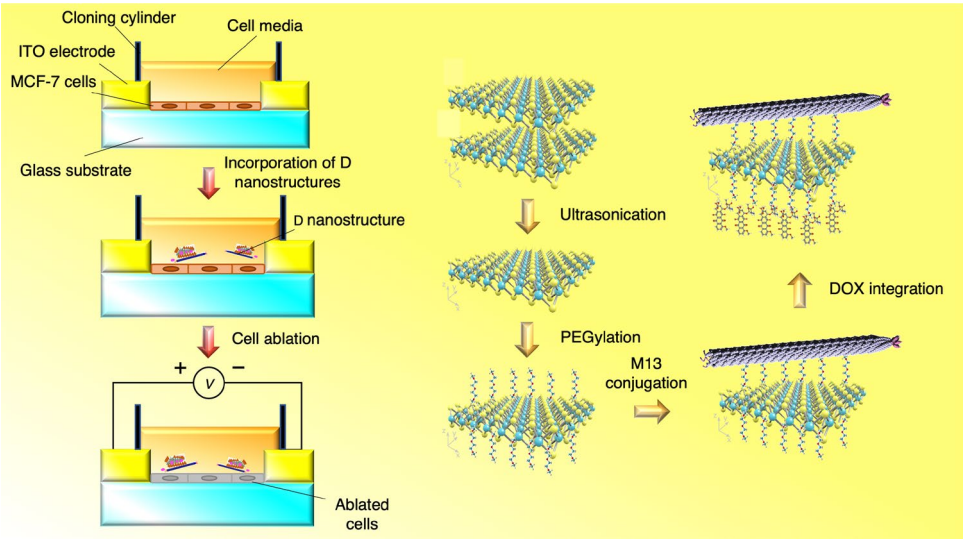

Keywords Thermal therapy · MCF-7 cancer cells · Chemotherapy · WS_2 · PEG · M13

1 Introduction

Cancer thermal therapy (TT), which utilizes thermal agents (TAs) to create local hyperprexia for thermal ablation of tumors, has demonstrated great promise in both clinical and preclinical tests, as a highly efficient therapeutic methodology [1, 2]. TT-based tumor ablation was successful in ~ 90% of patients in a recent clinical work, with no substantial side effects, adverse alterations in organ function or serious sequelae [3–5]. With these encouraging findings, along with the European clinical approval of iron oxide nanoparticles, i.e., Nanotherm® developed by Magforce, for TT, this therapy approach is anticipated to generate a major, if not revolutionary, clinical effect [6]. However, designing TAs with both strong thermal phenomena, viz., excellent thermal conversion effectiveness and/or thermal stability for effective therapeutic results, and quick degradability, e.g., rapid degradation to alleviate safety issues, remains difficult [7, 8].

A type of traditional TA utilized in preclinical investigations, i.e., inorganic nanomaterials, is based on nanoagents with excellent thermal stability when stimulated. However, TAs disintegrate with difficulty or slowly, generating concerns about biosafety and excretion [9, 10]. Another conventional TA with quick degradability, viz., clinically authorized indocyanine green, creates less safety and biocompatibility issues [11, 12]. However, fast deterioration undermines the thermal stability required for optimal therapeutic effectiveness. It was common for thermal function to be lost within a few seconds or upon recurrent stimulation [13–15]. Furthermore, input stimulation increases the breakdown of TAs. While increasing TA concentrations result in a stronger TT, it is associated with clinical issues including high renal and liver load [16, 17]. As a result, the contradiction between high thermal stability and quick degradation of traditional TAs is a substantial obstacle to TT achieving its therapeutic potential [18–20].

Tungsten disulfide (WS_2) has been integrated into functional TAs with various nanostructures as a biodegradable and biocompatible two-dimensional (2D) nanosized material [21–23]. However, traditional types of WS_2 nanostructures agglomerate in the presence of slats. As a result, the conventional WS_2 type is one of the TAs with low thermal stability [24, 25]. Chemical alterations have been implemented to increase the thermal or stability performance of prototypical WS_2 types, but the improvements come at the expense of protracted deterioration [26, 27]. The M13 is a non-lytic bacteriophage with specified proteins that is cylindrical in shape, 880 nm long and 5–6 nm in diameter [28–32]. Given that (i) the M13 phage is a promising candidate for next-generation cancer cell targeting agents, (ii) the polyethylene glycol (PEG) polymer can be utilized to coat WS_2 nanosheet surfaces through disulfide binding, which substantially increase the biocompatibility and physiological stability of the nanosheet, and (iii) the WS_2 nanosheet, which exhibits a

large surface-area-to-mass ratio, owing to its atomically thin 2D structure, may efficiently load the chemotherapy drug, doxorubicin (DOX), we hypothesis that the integration of DOX-conjugated WS_2 and PEG-combined M13 to generate DOX–WS_2–PEG–M13 nanostructures (we term them D nanostructures) may enhance the thermal performance, and at the same time, maintaining rapid degradation, for TT, and improve therapeutic outcomes for chemotherapy.

Herein, we demonstrate that by stimulating and altering the Joule heating process, we are able to modulate the thermal character of the WS_2 by using D nanostructures, and design an integrated system for TT to avoid the aforementioned drawbacks of TAs (Fig. 1), and chemotherapy to achieve effective treatment. The D-based TT (DTT) variety reveals a relative cell viability of 50%, in addition to a 1 nM drug concentration. The D-enabled chemotherapy (DCT) model also discloses a relative cell viability of 80% for 1 nM drug concentration, while a 1-week degradation time was exhibited by the D nanostructure. Theoretical works reveal the drug molecule–nanostructure and drug-on-nanostructure–solution interaction-assisted improvement in drug loading and drug release performance in DCT modes. Thus, we devised an effective technique to reconcile the hitherto unresolved conflict between thermal stability and fast degradation of TAs.

2 Materials and methods

2.1 Cell culture

Breast cancer cells (MCF-7) were grown in a 25 cm^2 culture flask in Dulbecco's modified Eagle's medium (DMEM) with L-glutamine (Nacalai Tesque) supplemented with 7% fetal bovine serum (FBS) (Gibco). The cell lines were maintained in a humidified atmosphere containing 5% CO_2 at 37 °C.

2.2 *Escherichia coli* (*E. coli*) and M13 phage propagation

The 5-alpha F'Iq competent *E. coli* (high efficiency) was purchased from New England Biolabs (NEB) as the host cell for M13 phage propagation. The bacteriophage M13 15669-B1 (M13 phage) was purchased from ATCC and revived according to the ATCC phage recovery and propagation protocol. *E. coli* overnight culture (O.C.) was then prepared with tetracycline (TET), followed by 4–6 h of incubation at 90 rpm on a shaker until the mixture became cloudy with an optical absorbance of

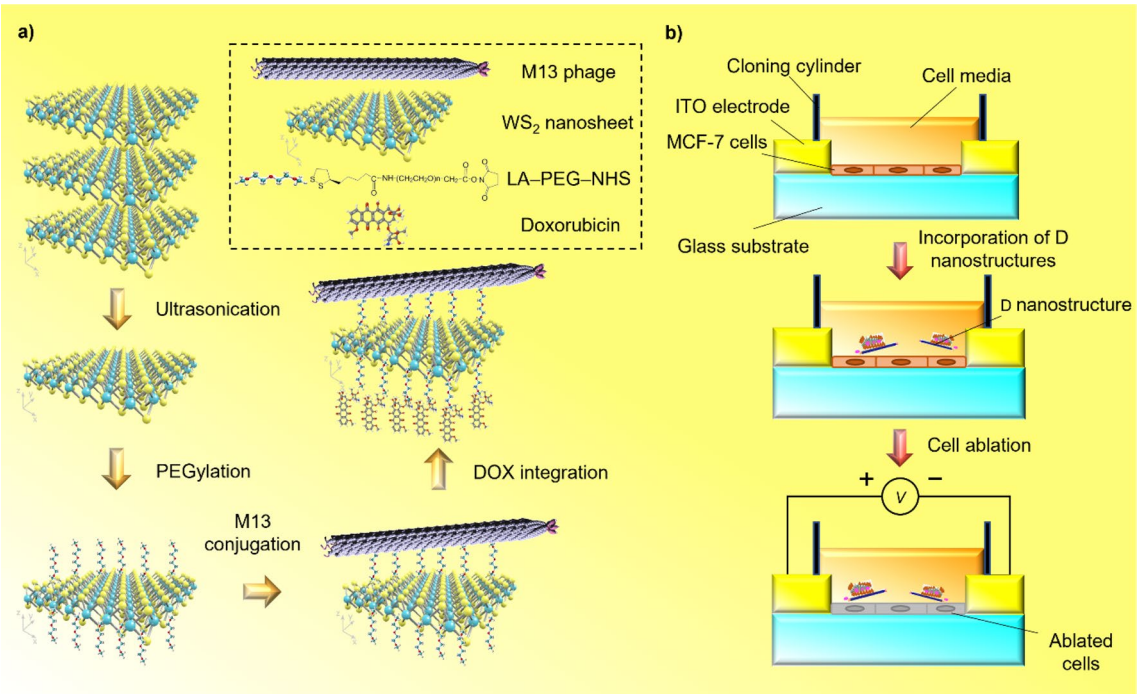

Fig. 1 A multifunctional system based on D nanostructures. **a** Depiction of the fabrication and composition of the D nanostructure. **b** The cellular response generated by the therapeutic effect of D nanostructures is illustrated

0.4 when measured at 600 nm (OD600). A new culture (N.C.) was formed by incubating the O.C. in Lennox L Broth Base (LB Broth Base) at 37 °C for 4–6 h at 90 rpm. The first and second precipitations were performed according to the manufacturer's M13 amplification protocol. The concentration of the M13 phage was then measured using a μDrop plate (Thermo Fisher Scientific Inc., Singapore).

2.3 WS_2–PEG–M13 material synthesis

The WS_2 in sterile, deionized water (DI water) was purchased from 2D Semiconductors, Inc. The lipoic acid (LA), PEG, and *N*-hydroxysuccinimide ester branches (NHS) (LA–PEG–NHS) were purchased from Nanocs Inc. and reconstituted in DI water. The WS_2 suspension was sonicated prior to use to form a homogenous mixture. Then, the LA–PEG–NHS was added to the WS_2 in DI water and the mixture was incubated on the shaker at 25 °C for 48 h with gentle shaking. The M13 phage was filtered to ensure sterility. The filtered M13 phage was then added to the mixture and incubated at 25 °C for 48 h with gentle shaking. Finally, the WS_2–PEG–M13 mixture was resuspended in Dulbecco's phosphate-buffered saline (DPBS).

2.4 Fabrication of DOX–WS_2–PEG–M13 material

Doxorubicin hydrochloride (DOX) was purchased from Selleckchem and the initial stock was diluted in water at 100 mg mL^{-1}. The WS_2–PEG–M13 mixture was diluted in DPBS. The DOX solution was then added to the WS_2–PEG–M13 mixture and incubated at 25 °C overnight. The next day, the DOX–WS_2–PEG–M13 mixture was centrifuged at 10,000 rpm for 10 min. The pellet was dissolved in 100 μL DPBS prior to fluorescence intensity experiments.

2.5 Fluorescence intensity measurement

Doxorubicin was prepared in DPBS at concentrations of 0, 5, 10, 15 and 20 μM. The variation of fluorescence intensity for different doxorubicin concentrations was examined. The samples were deposited in 96 well plates and the fluorescence intensity was measured using a Thermo Scientific Varioskan Lux microplate reader. The excitation wavelength was fixed at 495 nm and the emission wavelength was set to 535 nm. The results were plotted using a scatter plot (Supporting Fig. S1). Regression analysis was utilized to create a straight line using the equation

$$y = mx + c, \tag{1}$$

where y is the fluorescence intensity and x is the doxorubicin concentration. The R squared (R^2) value was calculated to determine the correlation strength between fluorescence intensity (y) and doxorubicin concentration (x). The R^2 value of 0.9968 in the chart disclose a strong correlation and suitability for use in this work.

2.6 Drug binding studies

Doxorubicin at 1.0, 5.0 and 10.0 μM concentrations was added to 10% and 30% DOX–WS_2–PEG–M13 mixtures. After an overnight incubation at 25 °C, the mixture was centrifuged and the fluorescence intensity was measured. The initial and bound drug concentrations were calculated using Eq. (1), and the bound drug percentage was denoted by

$$\textit{Bound drug percentage} = \frac{\textit{Bound drug concentration } (\mu M)}{\textit{Initial drug concentration } (\mu M)} \times 100\%. \tag{2}$$

2.7 The drug release study

1 μM Doxorubicin was added to a 30% DOX–WS_2–PEG–M13 mixture. After an overnight incubation at 25 °C, DPBS at different pH levels, i.e., 5.0 and 7.4, was added to the mixture. The mixture was centrifuged at 14,000 rpm for 15 min at specified intervals, and the pellet was dissolved in 100 μL DPBS prior to fluorescence intensity measurement. The bound drug concentration at the initial time and the bound drug concentration at the specified time were calculated based on Eq. (1), and the retained drug percentage was defined as

$$Retained\ drug\ percentage = \frac{Bound\ drug\ concentration\ at\ specified\ time(\mu M)}{Bound\ drug\ concentration\ at\ initial\ time\ (\mu M)} \times 100\%. \quad (3)$$

2.8 Material characterization

Fourier-transform infrared (FTIR) spectroscopy was performed using an infrared spectrometer (PerkinElmer, Shelton, CT, USA) after drop-casting the samples on a silicon (Si) substrate. The morphology of the WS_2 and DOX–WS_2–PEG–M13 samples was investigated using atomic force microscopy (AFM, Bruker Dimension Icon system). Samples were drop-casted on the Si substrate and examined using a 1.5 µm × 1.5 µm scan size. The sample thickness was measured using the Gwyddion software.

2.9 In vitro cytotoxicity study

Cells were seeded in 96 well plates and cultured for 24 h before treatment with different DOX, WS_2–PEG–M13, and DOX–WS_2–PEG–M13 nanostructure concentrations. The relative cell viability was defined as the percentage of living cells in a cell population and was determined using the crystal violet (CV) assay after 24 h of material incubation. The CV was generated by dissolving the powder in 0.05% methanol. The samples, i.e., cells treated with WS_2–PEG–M13 and cells treated with DOX–WS_2–PEG–M13, were washed using DPBS. The CV was then added to these samples, which were dried at room temperature overnight. The output absorbance of the samples was determined at λ = 570 nm using a multi-plate reader (Thermo Scientific Multiskan GO).

2.10 Electrothermal ablation studies

MCF-7 cells were seeded at a density of 3000 cells per well using indium tin oxide (ITO)-on-glass systems. The system comprised two 650 nm-thick left and right ITO electrodes on a glass substrate (Latech), with a cloning cylinder secured using a silicone adhesive (Sigma-Aldrich). The distance between the electrodes was 0.1 mm. To facilitate attachment to the glass surface, cells were cultured for 24 h. The cells were then treated with pristine DOX, bare WS_2–PEG–M13, and DOX–WS_2–PEG–M13. After 24 h, electrical stimuli with amplitudes of 1, 2, and 5 V and a length of 2 µs, and a total of 1000 bursts were administered to the system. In another experiment, the system was furnished with electrical stimuli with lengths of 1, 2, and 5 µs and an amplitude of 2.0 V, and a total of 1000 bursts. Additionally, a total of 500, 1000 and 2000 bursts, and electrical stimuli with a length of 2 µs and an amplitude of 2.0 V were injected to the system. Subsequently, the cell viability was examined using the CV assay 24 h after the stimuli were applied.

2.11 Thermal simulation

The ANSYS software was utilized to analyze the thermal distribution within the cell layer using the DOX–WS_2–PEG–M13 nanostructure model. The simulation parameters utilized were disclosed in Supplementary Table S1. Different stimulus amplitudes were administered to the system, ranging from 1.0 to 7.0 V. The corresponding peak temperatures in the cell layer for each stimulus amplitude were then determined. In another simulation, thermal distributions of the WS_2-in-DMEM model and DOX–WS_2–PEG–M13-in-DMEM model for different model states after 5 V stimulus were analyzed. The corresponding peak temperatures of the WS_2-DMEM model and DOX–WS_2–PEG–M13-in-DMEM model were then plotted to determine the nanostructure thermal stability.

2.12 Fluorescence imaging

After incubation with the DOX–WS_2–PEG–M13 mixture in ITO-on-glass systems, cells were fixed with 3.7% Paraformaldehyde (Sigma-Aldrich) at specified intervals for 10 min at room temperature and washed three times with DPBS. Following the removal of the DPBS, 0.1% Triton X 100 (Sigma-Aldrich) was applied. The 0.1% Triton X 100 was removed after 10 min, and the sample was rinsed three times with DPBS. After removing the DPBS, 2% FBS (Gibco) was added. Cells were incubated at room temperature for 2 h on a shaker at 70–80 rpm. The cells were then washed with DPBS and

the cloning cylinder was removed. Finally, 5 µL of DAPI mounting media (Invitrogen) was added, and the ITO-on-glass system was allowed to dry completely before imaging.

Doxorubicin fluorescence was detected using a confocal microscope (Olympus CKX Series). The ITO-on-glass system was examined at 40× objective magnification and digitally photographed to determine the doxorubicin uptake into the cells. The DAPI fluorescence associated with cell nuclei was stimulated by UV light at 360 nm, with an emission maximum at 460 nm, and was detected using a DAPI traditional filter. The Cy3 fluorescence corresponding to doxorubicin was visualized utilizing 561 nm excitation and 572–647 nm emission filter sets. The fluorescence images of DAPI and doxorubicin were merged using ImageJ software (NIH, Bethesda, MD).

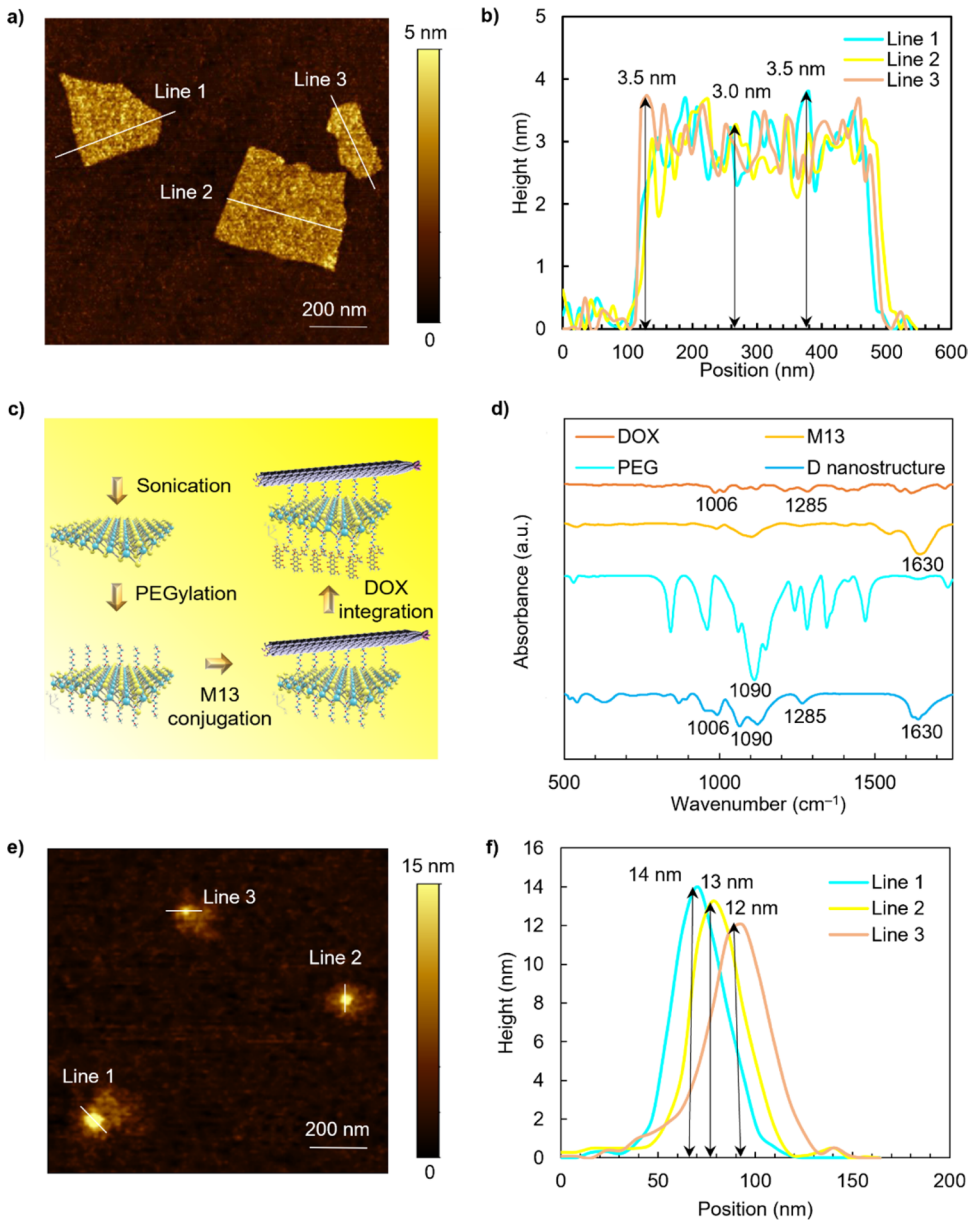

Fig. 2 D nanostructure characterization. **a** AFM image of WS_2 nanostructures. **b** Height profiles of the WS_2 nanostructure along the white lines in **a**. **c** Schematic illustration of the fabrication process of D nanostructures. **d** FTIR spectra of the D nanostructure, PEG, M13, and DOX. **e** AFM image of D nanostructures. **f** Height profiles of the D nanostructure along the white lines in **e**

3 Results and discussion

3.1 Synthesis and characterization of D nanostructures

Ultrasonication-enhanced liquid exfoliation of bulk WS_2 generates WS_2 nanosheets [33, 34]. The atomic force microscopy (AFM) image reveals that the WS_2 nanosheet exhibits an average lateral size of ~ 390 nm (Fig. 2a) and an average thickness of ~ 3 nm, suggesting a stack of one triple layer of WS_2 (Fig. 2b). We further modified the WS_2 nanosheet with PEG to improve the biocompatibility and stability [35, 36]. To confer cancer cell targeting capabilities to WS_2 nanosheets, a bacteriophage M13 with a high affinity to human epidermal growth factor receptor 2 (HER2), which is overexpressed on cancer cells, is conjugated to PEG molecules [28]. HER2 is a member of the epidermal growth factor receptor (EGFR)-based family of receptor tyrosine kinases (RTKs), which regulates cell proliferation and survival. Besides, HER2 overexpression is associated with vascular endothelial growth factor (VEGF) upregulation, which enhances angiogenesis and cancer metastases, leading to an unfavorable prognosis. As a result, HER2 is an attractive target for breast cancer therapeutics [37–42]. Moreover, experiments have demonstrated that phage-conjugated nanomaterials assemble on cancer cells. When a strong input stimulus is applied, the conductive nanomaterial generates an output temperature above 313 K via strong Joule heating, which results in cancer cell killing. The M13 was connected to PEG molecules through the amine reaction, and based on disulfide binding, the WS_2 nanosheet was attached to the PEG molecule [35, 43]. Additionally, the DOX was conjugated to PEG molecules using an amide linkage. The conjugation was performed by using a mixture of LA–PEG–NHS as a linker between the M13 and PEG molecules, as well as between the DOX and the PEG molecule. The NHS of the LA–PEG–NHS reacted with the amine group on the M13 phage, whereas the LA bound to the WS_2 nanosheet was driven by disulfide binding [43]. Moreover, the amine group on the DOX reacted with the NHS of the LA–PEG–NHS [44, 45]. Finally, D nanostructures were generated, as depicted in Fig. 2c. The Fourier transform infrared (FTIR) spectroscopy was also utilized to investigate the grafting of the LA–PEG–NHS on the WS_2 (Fig. 2d). The archetypal stretching vibration of the carbonyl group in the PEG at ~ 1090 cm^{-1} was revealed by the FTIR spectrum of the D nanostructure, indicating the surface presence of the PEG [46]. The AFM image discloses that the average lateral size of D nanostructures is ~ 60 nm (Fig. 2e), which is smaller than that of the WS_2 nanosheet. During PEGylation, the sonication procedure can partially break down the nanosheets, resulting in a decrease in the diameter of WS_2 nanosheets. The average thickness of the D nanostructure was ~ 13 nm, as disclosed in the cross-sectional plot (Fig. 2f), with an increase in the sample thickness induced by the M13 phage, PEG polymer coating, and DOX. Recent studies have reported that the M13 exhibits a thickness of ~ 6 nm, whereas a thickness of a few nm is demonstrated for the case of the PEG and DOX [32, 47, 48]. Moreover, simulations revealed that pristine D nanostructure-in-DMEM models exhibited higher thermal stability or performance compared to that of the WS_2-in-DMEM model with degradation (Supporting Fig. S2).

3.2 D nanostructure degradation effect, WS_2 thermal signature, and drug loading and release effects

Understanding the degree of degradation in D nanostructures is an important step towards realizing a safe cancer therapy. Recent studies have demonstrated that material samples incubated for a specific time exhibit a smaller absorbance than that of pristine material samples, indicating that material breakdown occurs [49, 50]. Figure 3a discloses the results of the D nanostructure incubated in a DMEM solution for different times. The normalized absorbance, which denotes the degree of degradation, is large, when a short incubation time, i.e., week 0, is utilized (Fig. 3b), which means that a negligible or low degree of degradation appears. For the case when the incubation time is intermediate, viz., week 1, a medium normalized absorbance arises. This means that the material sample exhibits material deterioration, resulting in moderate to high degree of degradation. The thermal signature of the WS_2 can be examined by analyzing the thermal distribution of the bulk WS_2 generated by administering a direct current (DC) stimulus to the material sample (Fig. 3c). When the DC stimulus was applied, the peak temperature was higher than that of the pristine material sample due to the strong Joule heating process. The output temperatures are high for regions close to the centre of the samples, whereas in the case of a region distant from the middle of the sample, a low output temperature results. Figure 3d shows the peak temperature of the bulk WS_2 for different stimulus amplitudes. The higher the stimulus amplitude, the larger the peak temperature revealed by the material sample.

To investigate the drug loading ability of the D nanostructure, we define the degree of connectivity between the drug molecule and nanostructures as the material concentration [51, 52]. The nanostructures including carbon

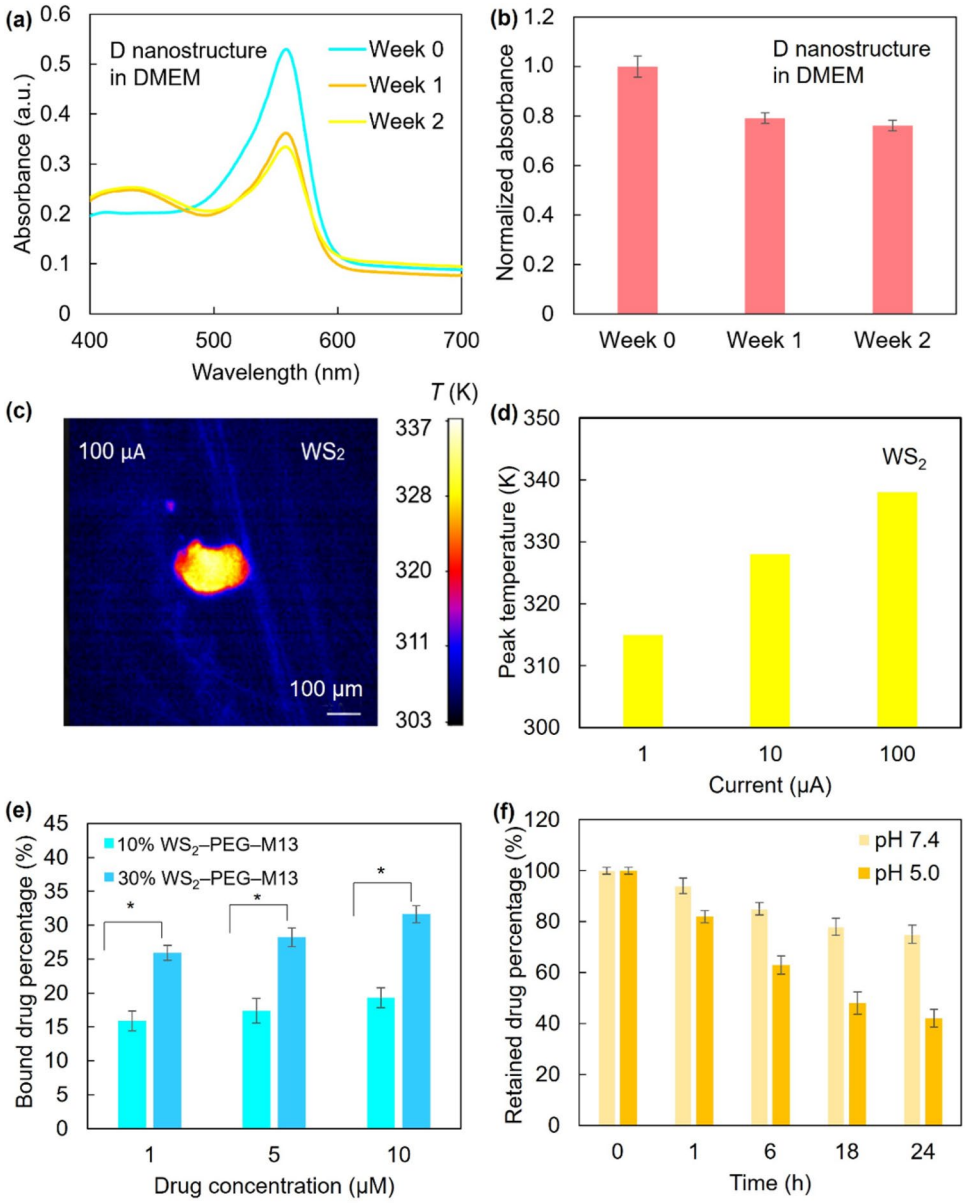

Fig. 3 Degradation effect of D nanostructures, WS_2 thermal character, and drug loading and release effects. **a** Absorbance spectra of the D nanostructure incubated in DMEM for different times. The D nanostructure concentration was fixed at 30% and 1 μM DOX was utilized. **b** Time evolution of the normalized absorbance of the D nanostructure in DMEM and at λ = 560 nm. **c** Thermographic map of the WS_2 sample after a direct current (DC) stimulus and with a peak temperature of 335 K. **d** Peak temperature variations in the bulk WS_2 sample for different stimulus amplitudes. **e** Variations in the loading capacities of DOX-combined WS_2–PEG–M13 nanostructures for different drug concentrations and WS_2–PEG–M13 concentrations. The significance values were calculated utilizing the Student's t-test and were marked as follows: *($p < 0.05$), **($p < 0.01$), ***($p < 0.001$), and ****($p < 0.0001$). Data are expressed as the standard error of the mean (SEM), where $n = 9$. **f** Drug release from the D nanostructure over time and at different pH levels. The DOX concentration was set at 1 μM and 30% D nanostructures were used

nanotubes, graphene and its derivatives with ultra-high surface areas, and sp^2-bonded carbon surfaces have been investigated as drug carriers for absorbing different types of drug molecules through π–π stacking and hydrophobic interactions [53–55]. Thus, a smaller material concentration corresponds to a lower degree of connectivity. Because we are interested in the variation of the interaction between the drug molecule and nanostructures, we record the alteration of the bound drug percentage. A clear dependence of the bound-drug percentage variation on the degree of connectivity and the drug concentration can be observed in Fig. 3e, with a high degree of connectivity being the most effective and a low degree of connectivity being the least effective. An upward trend in the bound drug percentage becomes manifest as the drug concentration increases owing to an increase in the degree of connectivity. This means that the nanostructure with a high degree of connectivity could induce strong drug molecule–nanostructure interactions and be utilized to absorb a large number of drug molecules, thus functioning as drug carriers [56, 57]. Moreover, a higher degree of connectivity should decrease the drug concentration necessary for achieving a targeted drug molecule–nanostructure interaction and enhance the drug loading process [55–58].

Recent studies have demonstrated that owing to the protonation of the amino group in the DOX molecule in an acidic solution, e.g., pH = 5.0, an enhanced DOX hydrophilicity and subsequent drug release from nanosheets results [59–61]. The degree of interconnectivity is defined as the variation in the interaction between the

drug-on-nanostructure and the solution. When the pH level of the test solution is low, a high degree of interconnectivity occurs, whereas a low degree of interconnectivity happens for the case when the pH level of the test solution is high [62, 63]. The D nanostructures were added to test solutions with different pH levels to examine drug-on-nanostructure–solution interactions. The retained drug percentage can be calculated by dividing the bound drug concentration at a specified time by the initial bound drug concentration, and multiplying the final value by 100%. After the material was added, retained drug percentages of the nanostructure were determined. The retained drug percentage as a function of time is depicted in Fig. 3f. When a high pH test solution is utilized, the retained drug percentage of the nanostructure remains high over time or the interaction between the drug-on-nanostructure and the solution is weak, resulting in the attainment of a low degree of interconnectivity. On the other hand, a high degree of interconnectivity arises for the case when a low pH test solution is applied.

3.3 Effects of D nanostructures on killing cancer cells

The influence of the WS_2–PEG–M13 nanostructure on the cytotoxicity was evaluated. The cytotoxicity of the WS_2 nanosheet is connected to surface processes. The degree of destructivity is low when a small material concentration is used, and for the case when a large material concentration is utilized, the degree of destructivity is high. The MCF-7 cells were incubated with WS_2–PEG–M13 nanostructures for 24 h to investigate the extent of cytotoxicity. After material

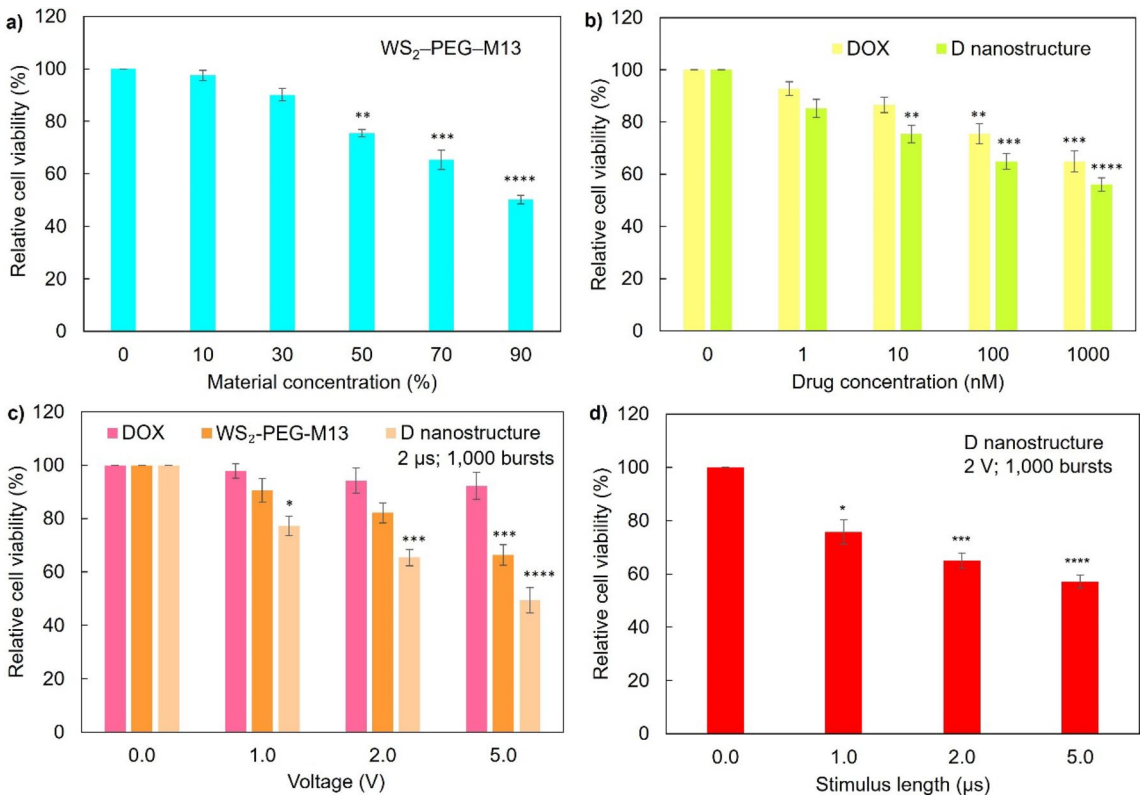

Fig. 4 The influence of D nanostructures on cancer cell destruction. **a** Variation in the relative viability of MCF-7 cells for different WS_2–PEG–M13 nanostructure concentrations. MCF-7 cells only were used as the control. **b** Variation in MCF-7 cell viability for varied DOX-incorporated WS_2–PEG–M13 nanostructure concentrations. MCF-7 cells with 30% WS_2–PEG–M13 nanostructures were utilized as the control. **c** The variation in the relative viability of MCF-7 cells with D, bare WS_2–PEG–M13, and pristine DOX nanostructures for different stimulus amplitudes. The MCF-7 cells with the D, bare WS_2–PEG–M13, and pristine DOX nanostructure were utilized as the control. The WS_2–PEG–M13 nanostructures was fixed at 30% concentration and 1 nM DOX was used. The relative cell viability was determined 24 h after the input stimulus. The significance values relative to control were calculated utilizing the Student's t-test and were marked as follows: *($p < 0.05$), **($p < 0.01$), ***($p < 0.001$), and ****($p < 0.0001$). Data are expressed as the standard error of the mean (SEM), where $n = 6$. **d** Variation in MCF-7 cell viability with D nanostructures for various pulse lengths. The MCF-7 cells with the D nanostructure were utilized as the control. The WS_2–PEG–M13 nanostructures was fixed at 30% concentration and 1 nM DOX was used. The relative cell viability was determined 24 h after the input stimulus. The significance values relative to control were calculated utilizing the Student's t-test and were marked as follows: *($p < 0.05$), **($p < 0.01$), ***($p < 0.001$), and ****($p < 0.0001$). Data are expressed as the standard error of the mean (SEM), where $n = 6$

incubation, the CV assay was administered to determine the viability of cell samples. The relative cell viability as a function of material concentrations is illustrated in Fig. 4a. When a small material concentration is applied, i.e., the material concentration is below 50%, the relative cell viability remains high or the extent of cytotoxicity is weak, resulting in the achievement of a low degree of destructivity. In contrast, a high degree of destructivity appears for the case when a large material concentration is implemented, e.g., above 50% material concentrations.

We utilized DOX as a model drug to investigate the potential of DOX-integrated WS_2–PEG–M13 nanostructures for delivering chemotherapy. Pure drug or high drug-concentration nano-carrier systems could enter cells in a non-specified manner, while endocytosis of nanostructures and intracellular release may be prolonged processes or disclose a low degree of destructivity, for the case of a low drug-concentration nano-carrier system [64–66]. The experiments utilized in this work revealed that cell viability stays high at WS_2–PEG–M13 nanostructure concentrations below 50%. Based on these findings, and to achieve high electrical conductivity and cell viability, we chose to utilize a WS_2–PEG–M13 nanostructure concentration of 30%. The relative viability of MCF-7 cells with DOX-combined WS_2–PEG–M13 nanostructures is assessed for different drug concentrations and the results are shown in Fig. 4b. The extent of cytotoxicity remains weak when a small drug concentration is used, viz., drug concentrations are below 10 nM. On the other hand, for the case when a high drug concentration is utilized, i.e., the drug concentration is above 10 nM, which means that nanostructures exhibit a high degree of destructivity, the nanostructure can be considered as cytotoxic, and a strong extent of cytotoxicity occurs. Moreover, experiments using pure DOX molecules have demonstrated that high drug concentrations are required to attain intermediate relative cell viability. On the other hand, when the DOX–WS_2–PEG–M13 nanostructure was added to the cells, the surface chemistry of the WS_2 nanosheet can lead to a level of toxicity that results in cell death. It is possible that the amount of DOX–WS_2–PEG–M13 nanostructures assembled on the cells at high drug concentrations is sufficient to induce cell death in a large cell population, resulting in low to intermediate cell viability.

An interesting phenomenon associated with cancer cell destruction is observed in D nanostructures. Experiments have disclosed that strong input stimuli are able to induce an output temperature above 313 K or a high degree of destructivity through strong Joule heating, leading to cancer cell death. The cancer cell killing effect is demonstrated in the nanostructure by applying input stimuli with different stimulus amplitudes. The relative cell viability remains high when the WS_2–PEG–M13 nanostructure concentration is below 50% and DOX concentrations are below 10 nM, as shown in the experiment utilized in this work. 30% WS_2–PEG–M13 nanostructures and 1 nM DOX were used, based on these results and to attain high cell viability and electrical conductance. The cancer cell destruction behaviour can be explained on the basis of the thermal signature of nanostructures [67–73]. The relative viability of the pristine cell sample is high, as shown in Fig. 4c, owing to the negligible Joule heating in the WS_2 nanosheet. For stimulus amplitudes between 0 and 2.0 V, which means that nanostructures have a low degree of destructivity, the nanostructure can be considered as unable to induce cancer cell killing, and a weak Joule heating results. However, the Joule heating becomes strong when the stimulus amplitude is above 2.0 V. Thus, the relative viability of the cell sample becomes low. Moreover, experiments showed that WS_2–PEG–M13 nanostructures were able to induce cell death in a medium cell population in response to high-amplitude stimuli. However, the input stimuli had negligible effect on the pristine DOX-induced cancer cell death. Additionally, the viability of WS_2–PEG–M13-treated cells decreases with increasing stimulus amplitude, from ~ 90% at 1.0 V to ~ 65% at 5.0 V. The D nanostructures, on the other hand, demonstrated excellent efficacy when incorporated with Joule heating, resulting in a cell viability of ~ 50% when the cells were injected with 5.0 V input stimuli. Besides, experiments with the bare D nanostructure revealed that the cells demonstrate a high relative cell viability. When an input stimulus is administered to the cells incubated with D nanostructures, the amplitude of the stimulus can lead to a temperature exceeding ~ 313 K, which results in cell death. However, the stimulus amplitude can be high enough to induce cell death in D nanostructure-treated cells for a large cell population, resulting in low relative cell viability. Similarly, input stimuli with increased pulse lengths and number of pulses, and D nanostructures with increasing material concentrations induce a higher degree of destructivity, leading to stronger Joule heating (Fig. 4d, Supporting Fig. S3). As shown in Supporting Fig. S4, the thermal distribution of the cell configuration was calculated by using electrothermal simulations. The simulation parameters were consistent with experimental conditions. Compared to the peak temperatures of cell models with low stimulus amplitudes, increased Joule heating was further observed based on the peak temperature of the cell mode with a high stimulus amplitude.

Notably, this work has disclosed the development of a previously unseen integrated system for chemotherapy and Joule heating-based thermal ablation, among state-of-the-art bare thermal therapy, chemotherapy-enhanced photothermal therapy and electrochemotherapy (Supporting Fig. S5, Table S2). This facilitates the destruction of a large cell population, enabling effective cancer therapy. Additionally, this work has exhibited the utilization of the WS_2–PEG nanostructure with M13 phage and the use of DOX drug molecules, which has not before been disclosed. It enables the

combination of chemotherapy and electrothermal therapy, which is of vital importance for avoiding multidrug resistance. Moreover, the work has demonstrated previously unreported theoretical studies of the drug molecule–nanostructure and drug-on-nanostructure–solution interaction-facilitated enhancement in drug loading and drug release performance in phage-polymer-nanosheet-drug material structures.

The phage, which assembles on the HER2 overexpressed on breast cancer cells, is integrated into the system to enhance therapeutic efficiency and enable nano-carrier specified cancer cell targeting. A high degree of specificity in nanostructures to assemble on cells occurs when cells and a phage-based nanostructure are utilized, and for the case when cells only are used, a negligible or low degree of specificity results. The cells, i.e., MCF-7 cells, were incubated with phage-based nanostructures, viz., the DOX–M13–WS_2–PEG, to investigate the assembly character of nanostructures. After material incubation, the cell sample was imaged using confocal fluorescence microscopy. The confocal fluorescent images for different cell samples, i.e., MCF-7 cells only and MCF-7 cells with DOX–M13–WS_2–PEG nanostructures, are depicted in Supporting Fig. S6. When cells with the phage-based nanostructure are used, the DOX fluorescence is strong or the nanostructure assembly on cells is high, resulting in the achievement of a high degree of specificity. In contrast, when cells only are harnessed, a negligible or low degree of specificity appears.

Owing to many constraints, applications such as an integrated system for chemotherapy and TT are extremely difficult for TA design. The constraints comprise: (i) low cell viability in TT, (ii) low drug concentration, (iii) short degradation time, and (iv) weak cell viability for chemotherapy only. Currently, none of the TAs available address all of the constraints specified above. According to the examples shown in this work, the current state of the integrated system appears to alleviate most of these constraints with a low cell viability in TT. The attained relative cell viability of ~ 50%, which is ~ 20 percentage points lower than the average of ~ 70% for existing combined systems for thermal-based therapy and chemotherapy (Supporting Fig. S7, Table S3), is a major enhancement in the DTT model that enables these applications. Thus, a large population of cancer cells are destroyed and an efficient cancer therapy is achieved. Additionally, experiments demonstrate that the DTT configuration exhibits a drug concentration of 1 nM, which is 99.8% smaller than the average of ~ 845 nM for state-of-the-art integrated systems for thermal-based therapy and chemotherapy (Supporting Fig. S8, Table S4). This allows the utilization of a small amount of materials, enabling low-cost cancer therapy. Moreover, the D nanostructure reveals a degradation time of 1 week, which is 75% shorter than the average of 4 weeks for current thermal-type agents (Supporting Fig. S9, Table S5). This allows the rapid discharge of TAs, enabling safe cancer therapy. Another important benefit of the hybrid system in this work is the low cell viability for pure chemotherapy. For example, the DCT mode discloses a relative cell viability of ~ 80% for 1 nM drug concentration, which is 15 percentage points smaller than the average of ~ 95% for state-of-the-art chemotherapy-based systems (Supporting Fig. S10, Table S6). This enables the destruction of a medium to large group of cancer cells with a low amount of materials for efficient, low-cost chemotherapy.

Electrothermal therapy (ETT) offers advantages over different thermal ablation techniques, e.g., photothermal therapy (PTT) and microwave thermal therapy (MWTT), due to its localized impact, high effectiveness, and minimal invasiveness to healthy tissue. ETT utilizes the combination of high voltage pulsed electric fields (PEF), dynamic energy delivery rates, and closed loop thermal control algorithms to rapidly generate focal ablations in a reproducible manner [74]. ETT allows automated adjustment of pulse delivery rate for temperature regulation in the ablation region, as well as modulating the delay between sequential waveforms based on real-time temperature measurements. This flexibility enables ETT to exhibit both non-thermal and controllable thermal configurations [75]. In clinical settings, this facilitates physicians in determining and regulating the extent of tumor destruction during treatment. Temperature-controlled points can be specifically positioned near designated tumors during treatment to ensure tissue preservation and protect critical structures from damage [76]. Therefore, ETT can effectively ablate tumor cells while preventing thermal injury in healthy tissues and minimizing treatment duration. On the other hand, photothermal therapy (PTT) is a methodology that utilizes photothermal agents to treat various diseases [77]. PTT applies thermal energy from light-to-heat conversion materials to efficiently destroy cancer cells. However, the effectiveness of prototypical photothermal agents has not been tested in large clinical trials. Thus, traditional laser ablation without photothermal agents has been utilized in clinical settings [78]. Conventional photothermal agents may also exhibit flaws that can hinder the effectiveness of PTT and lead to unintended consequences. The negative effects of archetypical PPT include normal tissue injury, insufficient thermal destruction of tumor sites, a short life span, and the poor penetration effect of excitation light sources [77]. Moreover, MWTT is an approach that utilizes electromagnetic fields to generate heat to destroy cancer cells through the rapid rotation of water molecules [79]. During breast tumor ablation, MWTT can preferentially kill breast tumour cells due to its higher water content compared to normal fatty breast tissue [80]. In clinical settings, the needle position and ablation

temperature are crucial safety predictors for conventional MWTT therapy. Recent studies on breast cancer lesions with thoracic metastases suggest that traditional MWTT treatment failures are primarily due to needle position [81]. Conventional MWTT systems' inadequate antenna design hindered ablation zone control and caused damage to healthy tissues surrounding the ablation zone. Prototypical MWTT systems' ablation-zone shape and size are also influenced by target tissue characteristics, leading to unpredictability. Archetypal MWTT systems further exhibit limitations in pain treatment, necessitating the use of anaesthesia [82]. Overall, ETT, due to its localized impact, high effectiveness, and minimal invasiveness to healthy tissue, is a promising alternative for cancer ablation treatment.

4 Conclusion

These low cell viability, as well as rapid degradation times are attained through the thermal signature of the WS_2, that alters the Joule heating process in D nanostructures. The DTT design attains a relative cell viability of 50%, as well as a 1 nM drug concentration. A relative cell viability of 80% for 1 nM drug concentration was also achieved by the DCT configuration, while the D nanostructure demonstrates a 1-week deterioration time. Theoretical investigations demonstrate the drug molecule–nanostructure and drug-on-nanostructure–solution interaction-assisted improvement in drug loading and drug release performance in DCT configurations. The D nanostructure is a unique TA idea with the potential to furnish a distinct solution to the trade-off between increasing thermal stability, and at the same time, increasing TA degradation. Given the excellent clinical potential of the TA and the substantial influence of the WS_2 in biomedical applications, this work opens the door for the prospective use of the WS_2 in chemotherapy-incorporated combination cancer therapy.

Acknowledgements We thank J. Y. Koh, A. H. Firdaus, Y. Lu and W. C. Teoh for valuable discussions. This work was financially supported by the Ministry of Education (Singapore) (MOE-T2EP50220-0022), SUTD-MIT International Design Center (Singapore), SUTD Kickstarter Initiative (SKI 2021_02_03, SKI 2021_02_17), SUTD-ZJU IDEA Grant Program (SUTD-ZJU (VP) 201903), Changi General Hospital (Singapore) (CGH-SUTD-HTIF2019-001), Agency of Science, Technology and Research (Singapore) (A20G9b0135) and National Supercomputing Centre (Singapore) (15001618).

Author contributions FSM planned the project and performed the experiments. MPM, SXG, LL, NB discussed the results and interpreted the data. DKL supervised the project.

Data availability The authors declare that data supporting the finding of this study are available within the article and the Supporting Information. Other data are available from the corresponding authors upon reasonable request.

Declarations

Competing interests The authors declare no competing interests.

References

1. Crezee J, Franken NAP, Oei AL. Hyperthermia-based anti-cancer treatments. Cancers. 2021;13(6):1240.
2. Oei AL, Kok HP, Oei SB, Horsman MR, Stalpers LJA, Franken NAP, Crezee J. Molecular and biological rationale of hyperthermia as radio- and chemosensitizer. Adv Drug Deliv Rev. 2020;163–164:84–97.
3. Elming PB, Sørensen BS, Oei AL, Franken NAP, Crezee J, Overgaard J, Horsman MR. Hyperthermia: the optimal treatment to overcome radiation resistant hypoxia. Cancers. 2019;11(1):60.
4. Debela DT, Muzazu SG, Heraro KD, Ndalama MT, Mesele BW, Haile C, Kitui SK, Manyazewal T. New approaches and procedures for cancer treatment: current perspectives. SAGE Open Med. 2021;9:205031212110343.
5. Liu R, Shen Q, Liu H. The efficacy and safety of thermal ablation for patients with lung malignancy: a meta-analysis of 12 studies in China. J Cardiothorac Surg. 2022;17:1.

6. Hu K, Xie L, Zhang Y, Hanyu M, Yang Z, Nagatsu K, Suzuki H, Ouyang J, Ji X, Wei J, et al. Marriage of black phosphorus and Cu^{2+} as effective photothermal agents for PET-guided combination cancer therapy. Nat Commun. 2020;11:2778.
7. Ouyang J, Feng C, Ji X, Li L, Gutti HK, Kim NY, Artzi D, Xie A, Kong N, Liu Y, et al. 2D monoelemental germanene quantum dots: synthesis as robust photothermal agents for photonic cancer nanomedicine. Angew Chem Int Ed. 2019;58:13405–10.
8. Tao W, Ji X, Xu X, Islam MA, Li Z, Chen S, Saw PE, Zhang H, Bharwani Z, Guo Z, et al. Antimonene quantum dots: synthesis and application as near-infrared photothermal agents for effective cancer therapy. Angew Chem Int Ed. 2017;56(39):11896–900.
9. Gao G, Sun X, Liang G. Nanoagent-promoted mild-temperature photothermal therapy for cancer treatment. Adv Funct Mater. 2021;31:2100738–2100738.
10. Zhang L, Forgham H, Shen A, Qiao R, Guo B. Recent advances in single Fe-based nanoagents for photothermal-chemodynamic cancer therapy. Biosensors. 2022;12:86.
11. Wu J, Williams GR, Niu S, Gao F, Tang R, Zhu LMA. Multifunctional biodegradable nanocomposite for cancer theranostics. Adv Sci. 2019;6:1802001.
12. Dai ZY, Shen C, Mi XQ, Pu Q. The primary application of indocyanine green fluorescence imaging in surgical oncology. Front Surg. 2023;10:1077492.
13. Teng CW, Huang V, Arguelles GR, Zhou C, Cho SS, Harmsen S, Lee JYK. Applications of idocyanine green in brain tumor surgery: review of clinical evidence and emerging technologies. Neurosurg Focus. 2021;50:E4.
14. Liu Y, Bhattaral P, Dai Z, Chen X. Photothermal therapy and photoacoustic imaging via nanotheranostics in fighting cancer. Chem Soc Rev. 2019;48:2053–108.
15. Zhao L, Zhang X, Wang X, Guan X, Zhang W, Ma J. Recent advances in selective photothermal therapy of tumor. J Nanobiotechnol. 2021;19:1.
16. Du B, Yu M, Zheng J. Transport and interactions of nanoparticles in the kidneys. Nat Rev Mater. 2018;3:358–74.
17. Peiravi M, Eslami H, Ansari M, Zare-Zardini H. Magnetic hyperthermia: potentials and limitations. J Indian Chem Soc. 2022;99: 100269.
18. Meivita MP, Lee D, Naikar JS, Go S-X, Teoh WH, Tan YS, Bajalovic N, Loke DK. An efficient, short stimulus PANC-1 cancer cell ablation and electrothermal therapy driven by hydrophobic interactions. Pharmaceutics. 2022;15:106–106.
19. Chan SSY, Go SX, Meivita MP, Lee D, Bajalovic N, Loke DK. Ultra-efficient highly-selective MFC-7 cancer cell therapy enabled by combined electric-pulse carbon 1D-nanomaterials platforms. Mater Adv. 2022;3:3915–24.
20. Du C, Wu X, He M, Zhang Y, Zhang R, Dong C. Polymeric photothermal agents for cancer therapy: recent progress and clinical potential. J Mater Chem B. 2021;9:1478–90.
21. Chen H, Liu T, Su Z, Shang L, Wei G. 2D transition metal dichalcogenide nanosheets for photo/thermo-based tumor imaging and therapy. Nanoscale Horiz. 2018;3:74–89.
22. Wang S, Zhao J, Yang H, Wu C, Hu F, Chang H, Li G, Ma D, Zou D, Huang M. Bottom-up synthesis of WS_2 nanosheets with synchronous surface modification for imaging guided tumor regression. Acta Biomater. 2017;58:442–54.
23. Chan SSY, Tan YS, Wu KX, Cheung, Loke DK. Ultra-high signal detection of human embryonic stem cells driven by two-dimensional materials. ACS Appl Bio Mater. 2018;1:210–5.
24. Bai J, Cui K, Xie X, Fang B, Wang F. Sepiolite-supported WS_2 nanosheets for synergistically promoting photocatalytic rhodamine B degradation. Catalysts. 2022;12:1400.
25. Peng K, Wang H, Li X, Wang J, Cai Z, Su L, Fan X. Emerging WS_2/montmorillonite composite nanosheets as an efficient hydrophilic photocatalyst for aqueous phase reactions. Sci Rep. 2019;9:16325.
26. Zhang C, Yong Y, Song L, Dong X, Zhang X, Liu X, Gu Z, Zhao Y, Hu Z. Multifunctional WS_2@poly(ethylene imine) nanoplatforms for imaging guided gene-photothermal synergistic therapy of cancer. Adv Healthc Mater. 2016;5:2776–87.
27. Yin W, Yan L, Yu J, Tian G, Zhou L, Zheng X, Zhang X, Yong Y, Li J, Gu Z, et al. High-throughput synthesis of single-layer MoS_2 nanosheets as a near-infrared photothermal-triggered drug delivery for effective cancer therapy. ACS Nano. 2014;8:6922–33.
28. Wang R, Li HD, Cao Y, Wang Z, Yang T, Wang J. M13 phage: a versatile building block for a highly specific analysis platform. Anal Bioanal Chem. 2023;415:3927–44.
29. Li L, Belcher AM, Loke DK. Simulating selective binding of a biological template to a nanoscale architecture: a core concept of a clamp-based binding-pocket-favored N-terminal-domain assembly. Nanoscale. 2020;12:24214–27.
30. Meivita MP, Go SX, Mozar FS, Li L, Tan YS, Bajalovic N, Loke DK. Shape complementarity processes for ultrashort-burst sensitive M13–PEG–WS_2-powered MCF-7 cancer cell sensors. Nanoscale. 2023;15:16658–68.
31. Dymova MA, Utkin YA, Dmitrieva MD, Kuligina EV, Richter V. Modification of a tumor-targeting bacteriophage for potential diagnostic applications. Molecules. 2021;26:6564–6564.
32. Bortot B, Apollonio M, Baj G, Andolfi L, Zupin L, Crovella S, di Giosia M, Cantelli A, Saporetti R, Ulfo L, et al. Advanced photodynamic therapy with an engineered M13 phage targeting EGFR: mitochondrial localization and autophagy induction in ovarian cancer cell lines. Free Radic Biol Med. 2022;179:242–51.
33. Yi H, Zhou X, Zhou C, Yang Q, Jia N. Liquid exfoliated biocompatible WS_2@BSA nanosheets with enhanced theranostic capacity. Biomater Sci. 2021;9:148–56.
34. Patrick DS, Bharathi P, Mohan MK, Muthamizchelvan C, Harish S, Navaneethan M. Liquid phase exfoliated WS_2 nanosheet-based gas sensor for room temperature NO_2 detection. J Mater Sci Mater Electron. 2021;33:9235–45.
35. Meivita MP, Chan SSY, Go SX, Lee D, Bajalovic N, Loke DK. WS_2/polyethylene glycol nanostructures for ultra-efficient MCF-7 cancer cell ablation and electrothermal therapy. ACS Omega. 2022;7:23075–82.
36. Long Y, Wu X, Li Z, Fan J, Hu X, Liu B. PEGylated WS_2 nanodrug system with erythrocyte membrane coating for chemo/photothermal therapy of cervical cancer. Biomater Sci. 2020;8:5088–105.
37. Wang J, Lamolinara A, Conti L, Giangrossi M, Cui L, Morelli MB, Amantini C, Falconi M, Bartolacci C, Andreani C, et al. HER2-displaying M13 bacteriophages induce therapeutic immunity against breast cancer. Cancers. 2022;14:4054.
38. Tarantino P, Morganti S, Curigliano G. Targeting HER2 in breast cancer: new drugs and paradigms on the horizon. Explor Target Anti-Tumor Ther. 2021;2:2.

39. Fang L, Yu Y, Li Y, Wang S, He J, Zhang R, Sun Y. Upregulation of AREG, EGFR, and HER2 contributes to increased VEGF expression in granulosa cells of patients with OHSS†. Biol Reprod. 2019;101:426–32.
40. Nasir A, Holzer TR, Chen M, Man MZ, Schade AE. Differential expression of VEGFR2 protein in HER2 positive primary human breast cancer: potential relevance to anti-angiogenic therapies. Cancer Cell Int. 2017;17:1.
41. Singh R, Kim WJ, Kim P-H, Hong HJ. Combined blockade of HER2 and VEGF exerts greater growth inhibition of HER2-overexpressing gastric cancer xenografts than individual blockade. Exp Mol Med. 2013;45:e52–e52.
42. Le X-F, Mao W, Lu C, Thornton A, Heymach JV, Sood AK, Bast RC Jr. Specific blockade of VEGF and HER2 pathways results in greater growth inhibition of breast cancer xenografts that overexpress HER2. Cell Cycle. 2008;7:3747–58.
43. Lee D, Chan SSY, Naikar JS, Meivita MP, Teoh WC, Bajalovic N, Loke DK. Ultrasensitive low-probe-concentration PANC-1 and MCF-7 cancer cell sensors enabled by combined 2D-material-polymer-phage frameworks. Mater Adv. 2023;4:291–301.
44. Hoelzer D, Leiske MN, Hartlieb M, Bus T, Pretzel D, Hoeppener S, Kempe K, Thierbach R, Schubert US. Tumor targeting with PH-responsive poly(2-oxazoline)-based nanogels for metronomic doxorubicin treatment. Oncotarget. 2018;9:22316–31.
45. Chen Q, Sowa DA, Cai J, Gabathuler R. Efficient one-pot synthesis of doxorubicin conjugates through its amino group to melanotransferrin P97. Synth Commun. 2003;33:2401–21.
46. Deygen IM, Kudryashova EV. New versatile approach for analysis of PEG content in conjugates and complexes with biomacromolecules based on FTIR spectroscopy. Colloids Surf B. 2016;141:36–43.
47. Chithrani DB. Polyethylene glycol density and length affects nanoparticle uptake by cancer cells. J Nanomed Res. 2014;1:1.
48. Lokerse WJM, Bolkestein M, Ten Hagen TLM, de Jong M, Eggermont AMM, Grüll H, Koning GA. Investigation of particle accumulation, chemosensitivity and thermosensitivity for effective solid tumor therapy using thermosensitive liposomes and hyperthermia. Theranostics. 2016;6:1717–31.
49. Gola D, Kriti A, Bhatt N, Bajpai M, Singh A, Arya A, Chauhan N, Srivastava S, Tyag PK, Agrawal Y. Silver nanoparticles for enhanced dye degradation. Curr Opin Green Sustain Chem. 2021;4: 100132.
50. Cavuslar O, Nakay E, Kazakoglu U, Abkenar SK, Ow-Yang CW, Acar HY. Synthesis of stable gold nanoparticles using linear polyethyleneimines and catalysis of both anionic and cationic azo dye degradation. Mater Adv. 2020;1:2407–17.
51. Zhuang W-R, Wang Y, Cui P-F, Xing L, Lee J, Kim D, Jiang H-L, Oh Y-K. Applications of π–π stacking interactions in the design of drug-delivery systems. J Control Release. 2019;294:311–26.
52. Khakpour E, Salehi S, Naghib SM, Ghorbanzadeh S, Zhang W. Graphene-based nanomaterials for stimuli-sensitive controlled delivery of therapeutic molecules. Front Bioeng Biotechnol. 2023;11:1129768.
53. Zainal-Abidin MH, Hayyan M, Ngoh GC, Wong WF. Doxorubicin loading on functional graphene as a promising nanocarrier using ternary deep eutectic solvent systems. ACS Omega. 2020;5:1656–68.
54. Chu KS, Schorzman AN, Finniss MC, Bowerman CJ, Peng L, Luft JC, Madden AJ, Wang AZ, Zamboni WC, DeSimone JM. Nanoparticle drug loading as a design parameter to improve docetaxel pharmacokinetics and efficacy. Biomaterials. 2013;34:8424–9.
55. Liu Y, Yang G, Jin S, Xu L, Zhao C. Development of high-drug-loading nanoparticles. ChemPlusChem. 2020;85:2143–57.
56. Cai K, He X, Song Z, Yin Q, Zhang Y, Uckun FM, Jiang C, Cheng J. Dimeric drug polymeric nanoparticles with exceptionally high drug loading and quantitative loading efficiency. J Am Chem Soc. 2015;137:3458–61.
57. Ali Y, Alqudah A, Ahmad S, Abd Hamid S, Farooq U. Macromolecules as targeted drugs delivery vehicles: an overview. Des Monomers Polym. 2019;22:91–7.
58. Manzari MT, Shamay Y, Kiguchi H, Rosen N, Scaltriti M, Heller DA. Targeted drug delivery strategies for precision medicines. Nat Rev Mater. 2021;6:351–70.
59. Hettiarachchi SD, Kirbas Cilingir E, Maklouf H, Seven ES, Paudyal S, Vanni S, Graham RM, Leblanc RM. PH and redox triggered doxorubicin release from covalently linked carbon dots conjugates. Nanoscale. 2021;13:5507–18.
60. Wang Y, Xu Z. Interaction mechanism of doxorubicin and SWCNT: protonation and diameter effects on drug loading and releasing. RSC Adv. 2016;6:314–22.
61. Dos Reis SB, de Oliveira SJ, Garcia-Fossa F, Leite EA, Malachias A, Pound-Lana G, Mosqueira VCF, Oliveira MC, de Barros ALB, de Jesus MB. Mechanistic insights into the intracellular release of doxorubicin from PH-sensitive liposomes. Biomed Pharmacother. 2021;134: 110952.
62. Hervault A, Dunn AE, Lim M, Boyer C, Mott D, Maenosono S, Thanh NTK. Doxorubicin loaded dual PH- and thermo-responsive magnetic nanocarrier for combined magnetic hyperthermia and targeted controlled drug delivery applications. Nanoscale. 2016;8:12152–61.
63. Wibowo FR, Saputra OA, Lestari WW, Koketsu M, Mukti RR, Martien R. PH-triggered drug release controlled by poly(styrene sulfonate) growth hollow mesoporous silica nanoparticles. ACS Omega. 2020;5:4261–9.
64. Sousa de Almeida M, Susnik E, Drasler B, Taladriz-Blanco P, Petri-Fink A, Rothen-Rutishauser B. Understanding nanoparticle endocytosis to improve targeting strategies in nanomedicine. Chem Soc Rev. 2021;50:5397–434.
65. Ding J, Shi F, Li D, Chen L, Zhuang X, Chen X. Enhanced endocytosis of acid-sensitive doxorubicin derivatives with intelligent nanogel for improved security and efficacy. Biomater Sci. 2013;6:633–46.
66. Mitchell MJ, Billingsley MM, Haley RM, Wechsler ME, Peppas NA, Langer R. Engineering precision nanoparticles for drug delivery. Nat Rev Drug Discov. 2020;20:1–24.
67. Rembiałkowska N, Dubińska-Magiera M, Sikora A, Szlasa W, Szewczyk A, Czapor-Irzabek H, Daczewska M, Saczko J, Kulbacka J. Doxorubicin assisted by microsecond electroporation promotes irreparable morphological alternations in sensitive and resistant human breast adenocarcinoma. Cells Appl Sci. 2020;10:2765.
68. Wężgowiec J, Kulbacka J, Saczko J, Rossowska J, Chodaczek G, Kotulska M. Biological effects in photodynamic treatment combined with electropermeabilization in wild and drug resistant breast cancer cells. Bioelectrochemistry. 2018;123:9–18.
69. Agnass P, Rodermond HM, van Veldhuisen E, Vogel JA, ten Cate R, van Lienden KP, van Gulik TM, Franken NAP, Oei AL, Kok HP, et al. Quantitative analysis of contribution of mild and moderate hyperthermia to thermal ablation and sensitization of irreversible electroporation of pancreatic cancer cells. J Therm Biol. 2023;115: 103619.
70. Batista Napotnik T, Polajžer T, Miklavčič D. Cell death due to electroporation—a review. Bioelectrochemistry. 2021;141: 107871.

71. Serio F, Silvestri N, Kumar Avugadda S, Nucci GEP, Nitti S, Onesto V, Catalano F, D'Amone E, Gigli G, del Mercato L, et al. Co-loading of doxorubicin and iron oxide nanocubes in polycaprolactone fibers for combining magneto-thermal and chemotherapeutic effects on cancer cells. J Colloid Interface Sci. 2022;607:34–44.
72. Terasaki A, Kurokawa H, Ito H, Komatsu Y, Matano D, Terasaki M, Bando H, Hara H, Matsui H. Elevated production of mitochondrial reactive oxygen species via hyperthermia enhanced cytotoxic effect of doxorubicin in human breast cancer cell lines MDA-MB-453 and MCF-7. Int J Mol Sci. 2020;21:9522.
73. O'Brien TJ, Lorenzo MF, Zhao Y, Neal RE, Robertson JL, Goldberg SN, Davalos RV. Cycled pulsing to mitigate thermal damage for multi-electrode irreversible electroporation therapy. Int J Hyperthermia. 2019;36:952–62.
74. Martin RC, McFarland K, Ellis S, Velanovich V. Irreversible electroporation in locally advanced pancreatic cancer: potential improved overall survival. Ann Surg Oncol. 2013;20:443–9.
75. Sano MB, Fesmire CC, Petrella RA. Electro-thermal therapy algorithms and active internal electrode cooling reduce thermal injury in high frequency pulsed electric field cancer therapies. Ann Biomed Eng. 2021;49:191–202.
76. Sano MB, Petrella RA, Kaufman JD, et al. Electro-thermal therapy: microsecond duration pulsed electric field tissue ablation with dynamic temperature control algorithms. Comput Biol Med. 2020;121: 103807.
77. Deng X, Shao Z, Zhao Y. Solutions to the drawbacks of photothermal and photodynamic cancer therapy. Adv Sci. 2021;8:2002504.
78. Li X, Lovell JF, Yoon J, Chen X. Clinical development and potential of photothermal and photodynamic therapies for cancer. Nat Rev Clin Oncol. 2020;17:657–74.
79. Carriero S, Lanza C, Pellegrino G, Ascenti V, Sattin C, Pizzi C, Angileri CA, Biondetti P, Ianniello PA, Piancientino F, Lavorato R, Ierardi AM, Carrafiello G. Ablative therapies for breast cancer: state of art. Technol Cancer Res Treat. 2023;22:15330338231157192.
80. Roubidoux MA, Yang W, Stafford RJ. Image-guided ablation in breast cancer treatment. Tech Vasc Interv Radiol. 2014;17:49–54.
81. Liu B, Wu Z, Mo H, He J, Lin X, Guan J, Wei C, Yuan Z. Safety and efficacy of microwave ablation for breast cancer thoracic metastases. Cancer Manag Res. 2018;10:5685–9.
82. Liu SX, Dalal S, Kruecker J. Automated microwave ablation therapy planning with single and multiple entry points. Proc SPIE. 2012;8316:945–52.